Local Reaction Environment Deviations within Gas Diffusion Electrode Pores for CO$_2$ Electrolysis

Butt, Esaar N.; Padding, Johan T.; Hartkamp, Remco

The Electrochemical Society
Advancing solid state & electrochemical science & technology

Local Reaction Environment Deviations within Gas Diffusion Electrode Pores for CO_2 Electrolysis

To cite this article: Esaar N. Butt *et al* 2024 *J. Electrochem. Soc.* **171** 014504

View the article online for updates and enhancements.

Local Reaction Environment Deviations within Gas Diffusion Electrode Pores for CO$_2$ Electrolysis

Esaar N. Butt, Johan T. Padding, and Remco Hartkamp[z]

Department of Process and Energy, Delft University of Technology, Delft, 2628 CB, The Netherlands

The local conditions inside a gas diffusion electrode (GDE) pore, especially in the electrical double layer (EDL) region, influence the charge transfer reactions and the selectivity of desired CO$_2$ER products. Most GDE computational models ignore the EDL or are limited in their applicability at high potentials. In this work, we present a continuum model to describe the local environment inside a catalytic pore at varying potentials, electrolyte concentrations and pore diameters. The systems studied in this work are based on an Ag catalyst in contact with KHCO$_3$ solution. Our study shows that steric effects dominate the local environment at high cathodic potentials ($\ll -25$ mV vs pzc at the OHP), leading to a radial drop of CO$_2$ concentration. We also observe a drop in pH value within 1 nm of the reaction plane due to electrostatic repulsion and attraction of OH$^-$ and H$^+$ ions, respectively. We studied the influence of pore radii (1–10 nm) on electric field and concentrations. Pores with a radius smaller than 5 nm show a higher mean potential, which lowers the mean CO$_2$ concentration. Pores with a favourable local environment can be designed by regulating the ratio between the pore radius and Debye length.

With the growing awareness of the impact of climate change, the demand for cleaner and non-fossil fuel-based energy sources is also increasing, and storing renewable energy over a long period of time is becoming of utmost importance. In this regard, CO$_2$ electrochemical reduction (CO$_2$ER) is one of the most attractive technologies to replace fossil fuels.[1–3] This process results in the formation of molecules that can be utilized as fuels and as chemical feedstock in various industries such as pharmaceutical, cosmetic, and plastic.[4–6] Although extensive research has been performed to make the CO$_2$ER process commercially viable, large-scale implementation is still not possible due to the inherent complexity of the process.

Conventional metal electrode cells are limited in their applicability due to severe mass transfer limitations for CO$_2$. Gas diffusion electrodes (GDE) overcome the limitation by delivering CO$_2$ in the gas phase directly to the catalytic pore in contact with the electrolyte.[7] This significantly reduces the distance CO$_2$ has to travel and has been shown to increase the current densities of desired CO$_2$ER reactions.[8,9]

Optimal design of a GDE is at the forefront of CO$_2$ER research. Most of the experimental research in this field focuses on the optimization of catalyst metal composition.[7,10] The goal is generally to optimize for stability and selectivity of the desired CO$_2$ER products;[11] however, because of the small length scales involved in such an electrochemical cell configuration, it is extremely challenging to probe the local environment inside a pore using experimental techniques. Continuum models are a cheap and reliable alternative to not only study the GDEs but also to optimize their design. The main interest in CO$_2$ER models lies in the cathodic half of the cell, where the CO$_2$ER process takes place.[12–17] The cathodic GDE is made up of a macroporous gas diffusion layer (GDL) for the distribution of CO$_2$ from the gas inlet to the catalytic pores and for the transport of products from the catalytic pores to the outlet stream. A hydrophobic microporous layer (MPL) composed of carbon nanoparticles is deposited on top of the GDL, acting as a current collector and barrier for the liquid electrolyte. The catalyst nanoparticle layer (CL) is coated directly on top of the MPL. Gaseous CO$_2$ is introduced via an inlet stream that flows along the GDL. It passes through the GDL/MPL sections to reach the catalyst layer where the reaction takes place. The aqueous electrolyte is circulated via the electrolyte flow channel alongside the catalyst layer.

Most of the research on GDE flow cells is based on one-dimensional (1D) models that do not incorporate the influences of pore size on the local reaction environment[8,18–20] and thus are unable to capture the complete spatial variation in the concentration. Some models assume an infinitely thin CL in contact with the electrolyte, hence bypassing the modelling of ion transport inside the CL.[21] There have been some attempts to include the 2D effects along the flow channel; however, such models often do not account for pore-scale transport[22] or do not consider the influence of steric effects on the local concentrations and pH profiles.[23,24] Furthermore, most of these models assume electroneutrality throughout the simulation domain. This condition is generally valid for modelling the transport of solution species within the diffusion layer. However, this is not valid for transport within the diffuse layer of the electric double layer (EDL). This region is defined by charge separation which results in large concentration gradients near the pore wall. This local environment within the catalytic pore is a key factor determining the overall performance and selectivity of desired products.[25–28] Bohra et al.[29] attempted a pore-scale model that did consider the EDL and steric effects inside a nanopore; however, the authors faced numerical instability beyond a potential value of -25 mV vs pzc on the outer Helmholtz plane (OHP). This severely limited the descriptive capabilities of their model as many industrially relevant CO$_2$ER reactions become thermodynamically favoured at higher potential ranges.[30]

In this work, we present an approach to model the CO$_2$ER process inside a single cylindrical nanopore of a GDE-based electrolyzer. We use the size-modified Poisson-Nernst-Planck (SMPNP) framework as described in our previous work for a flat metal-based electrode system and modify it for a GDE nanopore.[31] Our aim with this study is to highlight the variation in the predicted local properties inside a nanopore due to changes in key performance-controlling parameters such as the size of the pore, electrolyte concentration, and the applied electrode potential. We first highlight the influence of the applied potential on the concentration profiles of solution species inside a nanopore. By doing so, we emphasize the importance of steric effects for such nanoporous spaces in CO$_2$ER. We then point out the radial trend of the local pH and show its variation with applied potential. We also show a strong influence of ionic strength on the amount of dissolved CO$_2$ inside the nanopore. Finally, we highlight the effect of pore size on the local reaction environment and demonstrate the importance of the ratio between the pore radius R and the Debye length λ_{Debye} in regulating the pH behavior inside a nanopore.

[z]E-mail: r.m.hartkamp@tudelft.nl
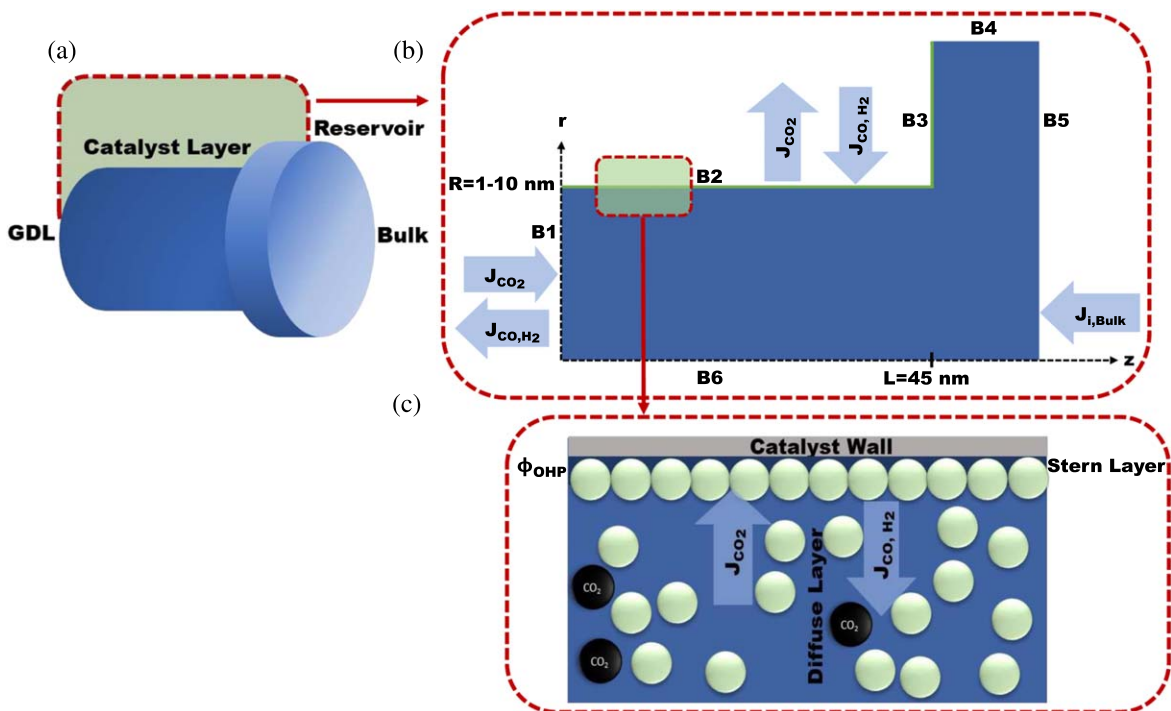
Figure 1. (a) Schematic of an idealized catalyst layer in the shape of a cylindrical pore along with reservoir section. (b) 2D simulation domain based on the axisymmetry condition. (c) A zoomed-in visual of the catalyst pore wall including cation-bound Stern and Diffuse layer. The reservoir section has width = 5 nm and a height of height = R + 5 nm. B1 to B6 represent the boundaries of the simulation domain.

Model Description

Figure 1a illustrates the idealized CL, assumed to be in the shape of an axisymmetric cylindrical nanopore. Since the studied catalyst pores are very small (1-10 nm) and hydrophilic, they are completely flooded by electrolyte.[18,29] The pore entrance on the left-hand side serves as the location of gas/liquid interface. The model is adopted for an Ag(111)-based catalytic pore. Silver is chosen because it is one of the more extensively researched metals in GDE-based CO_2ER studies due to its high selectivity toward CO.[18,29,32] The axisymmetric pore is conveniently described in a two-dimensional model (Fig. 1b). Furthermore, we introduce a reservoir section at the right-hand side of the domain between the pore and the bulk electrolyte region. The reservoir section not only allows for a realistic transport of solution species into the catalyst layer but it also facilitates numerical convergence by allowing a gradual development of ionic concentration profiles at high applied potentials, thus enhancing stability. The risk of instability is highest at the pore entrance near the reaction plane B2. By applying the same potential on the reservoir wall B3 as on the reaction plane B2 (Fig. 1b), we allow a smooth gradient in the potential fields which makes the overall system numerically stable even at high applied potentials. The applied potential ranges from −0.12 to −0.3 V vs pzc at the OHP. The boundaries in the reservoir section do not take part in the CO_2ER reactions. The transport Eqs. and the homogeneous reactions are solved throughout the simulation domain.

$KHCO_3$ is chosen as the electrolyte in this work because it is one of the most commonly used electrolytes in Ag-based CO_2ER processes.[18,29,32] The following homogeneous equilibrium reactions occur in the electrolyte:

$$HCO_3^- + OH^- \underset{k_{-1}}{\overset{k_1}{\rightleftharpoons}} CO_3^{2-} + H_2O, \qquad [1]$$

$$CO_2 + OH^- \underset{k_{-2}}{\overset{k_2}{\rightleftharpoons}} HCO_3^-, \qquad [2]$$

$$H_2O \underset{k_{-3}}{\overset{k_3}{\rightleftharpoons}} H^+ + OH^-. \qquad [3]$$
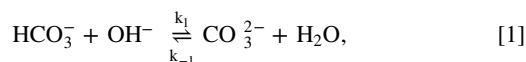
Here, k_n and k_{-n} are the forward and backward rate constants, respectively. All the rate constant values are listed in the supplementary information (Table S2). The model solves for the mass transport of the following 8 species: CO_2, CO, OH^-, H_2, HCO_3^-, K^+, CO_3^{2-} and H^+ throughout the simulation domain (Fig. 1b). The following set of SMPNP equations (Eqs. 4–7) is used to model the transport:

$$\frac{\partial C_i}{\partial t} = \nabla \cdot \left[D_i \nabla C_i + \frac{D_i C_i z_i F}{RT} \nabla \Phi \right.$$
$$\left. + D_i C_i \left(\frac{\beta_i N_A \sum_{j=1}^n a_j^3 \nabla C_j}{1 - N_A \sum_{j=1}^n a_j^3 C_j} \right) \right] + \sum_s R_i. \qquad [4]$$

C_i represents the concentration of solution species i. z_i is the valency of species i, a_j represents the effective hydrated size of all ionic species. However, for $j = CO_2$, a_j represents the size of the unhydrated CO_2 molecule because CO_2 has a very weak solvation shell in polar solvents. Φ is the local electric potential. F is Faraday's constant, R is the gas constant, T represents the absolute temperature of the system and N_A is Avogadro's number. R_i represents the formation rate for species i in the homogeneous reactions (Eqs. 1–3) (see supplementary information for detailed methodology). D_i is the diffusivity of species i. Values of all diffusivities and sizes of all the solution species are given in the supplementary information (Tables S4 and S5, respectively). The first two terms on the right-hand side of Eq. 4 are the diffusion and migration terms, respectively. The third term comes from the excluded volume effect.[33–38] The β_i factor in the excluded volume term is given by:

$$\beta_i = \frac{a_i^3}{a_0^3}. \qquad [5]$$

Here, a_0 is the effective size of H_2O molecules. β_i acts as a magnification factor for the steric repulsion acting on species i inside the solution (Refs. 31, 39, 40). Equation 4 is solved self-consistently with the Poisson equation:

$$\nabla \cdot (\epsilon_0 \epsilon_r \nabla \Phi) = -F \sum_{i=1}^{n} z_i C_i. \qquad [6]$$

Here, ϵ_0 is the permittivity of the vacuum and ϵ_r is the relative permittivity of the aqueous electrolyte. ϵ_r varies with the local cation concentration (K^+, H^+)[27,41,42] and it is evaluated at every time step:

$$\epsilon_r = \epsilon_r^0 \left[\frac{M_{H_2O} - \sum_i^{n_{cat}} w_i C_i}{M_{H_2O}} \right] + \epsilon_r^{min} \left[\frac{\sum_i^{n_{cat}} w_i C_i}{M_{H_2O}} \right]. \qquad [7]$$

M_{H_2O} and ϵ_r^0 represent the molarity and the permittivity of pure water at room temperature. w_i is the number of cation-bound water molecules. ϵ_r^{min} is the dielectric constant of water under the condition of dielectric saturation.[41,42] Based on the Gouy-Chapman-Stern theory for the EDL, an immobile layer of adsorbed cations is formed at the pore wall due to an applied surface potential. This layer is called the Stern layer and its thickness is assumed to be slightly larger than the radius of a solvated K^+ ion ($\approx$0.4 nm).[27] Consequently, the outer Helmholtz plane (OHP) marks the plane of closest approach for the solution species and also the CO_2ER reaction plane. The potential drop across the Stern layer is often a modelling parameter as it requires assuming the relative permittivity and thickness of the Stern layer, both of which are hard to measure experimentally. A mixed Robin boundary condition based on the experimental data on Stern layer capacitance under similar conditions can be used to calculate the drop.[43] Since this work mainly focuses on resolving the local environment within the diffuse layer, we fix the potential values at the OHP rather than at the electrode. Note that the OHP corresponds to boundary B2 in Fig. 1b, and that therefore the radius R of the simulation domain is slightly smaller than the physical pore radius. The electrochemical reactions occurring at B2 are as follows:

$$CO_2(aq) + H_2O + 2e^- \rightleftharpoons CO(g) + 2OH^-, \qquad [8]$$

$$2H_2O + 2e^- \rightleftharpoons H_2(g) + 2OH^-. \qquad [9]$$
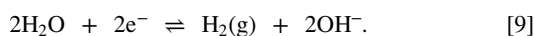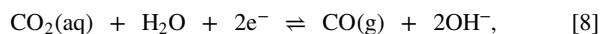
The mass transport model presented in this work can also be used for CO_2ER processes based on other catalytic metals such as Cu, Sn and In. This can be achieved by accounting for heterogeneous reactions and products specific to the catalyst being used, instead of Ag (111) (Eqs. 8 and 9). The next subsections detail the boundary conditions implemented in the simulation domain.

Gas/Liquid interface (B1).—This boundary exists at the interface of the MPL and the CL. The inlet gas stream passes through the GDL/MPL region to reach the gas/liquid interface B1. The flux of all solution species, except CO_2, CO and H_2, is assumed to be 0.

$$J_i = 0, \qquad i = HCO_3^-, K^+, H^+, OH^-, CO_3^{2-}. \qquad [10]$$

The CO and H_2 concentrations at the B1 boundary are determined by the following Dirichlet boundary condition:

$$C_i^{B1} = H_i p_1 y_i \rho_{elec}, \qquad i = CO, H_2. \qquad [11]$$

Here, H_i is Henry's constant, p_1 is the gas stream pressure and ρ_{elec} is the electrolyte density, taken to be the density of water. y_i is the

gas phase fraction of species i (Table S7). For CO_2, a Neumann flux condition based on Sechenov-corrected Henry's law is used.[8,29,44,45]

$$J_{CO_2}^{B1} = \kappa_{B1}(C_{CO_2}^{B1} - C_{CO_{2(aq)}}). \qquad [12]$$

Here, $C_{CO_2}^{B1}$, is the saturated concentration of CO_2, evaluated at every time step using the Sechenov-corrected Henry's relation (see supplementary document for the methodology). $C_{CO_{2(aq)}}$ is the local concentration of CO_2 inside the pore. κ_{B1}, is the gas/liquid interface mass transfer coefficient and is calculated based on film theory.[8,23]

$$\kappa_{B1} = \frac{D_{CO_2}}{\sigma}. \qquad [13]$$

Here, the film thickness (σ) depends on the level of saturation (S) inside the pore:[8,18]

$$\sigma = \frac{d_p}{2}(1 - \sqrt{1 - S}). \qquad [14]$$

A zero electric field condition is adopted for the B1 interface:

$$\nabla \Phi = 0. \qquad [15]$$

Reaction plane (B2).—The flux of the species involved in the charge transfer reactions at OHP (r = R) and time t is given by:

$$J_{i,(OHP,t)} = \sum_p \frac{\nu_{i,p} I_{ECSA} FE_p}{n_p F}, \qquad i = CO_2, H_2, CO, OH^-. \qquad [16]$$

$\nu_{i,p}$ represents the stoichiometric coefficient for species i in reaction p (Eqs. 8 and 9). n_p is the number of overall electrons transferred in reaction p. I_{ECSA} is the current density of the electrochemically active surface area and is calculated as:[29]

$$I_{ECSA} = \frac{I_{GEOM}}{f_r}. \qquad [17]$$

I_{GEOM} is the geometric current density and f_r is the electrode roughness factor. The electrochemically active surface area increases with increasing roughness of the electrode. f_r depends on the type of catalyst material used as well as the thickness of CL. FE_p is the Faradaic efficiency of reaction p.

For the species that do not take part in the charge transfer reactions:

$$J_{i,(OHP,t)} = 0, \qquad i = CO_3^{2-}, K^+, HCO_3^-, H^+. \qquad [18]$$

The fixed potential at the OHP is given by:

$$\Phi_{OHP} = E_{App}. \qquad [19]$$

Bulk electrolyte/pore interface (B5).—The flux of species i depends on the concentration difference between interface B5 and the bulk electrolyte:

$$J_i^{B5} = \kappa_{B5_i}(C_{i_{B5}} - C_{i_{BULK}}), \qquad i = CO_2, CO, H_2, OH^-, CO_3^{2-}, K^+, HCO_3^-, H^+. \qquad [20]$$

Here, $C_{i_{B5}}$ and $C_{i_{BULK}}$ are the concentrations of species i at the interface B5 and the bulk of electrolyte, respectively. The bulk concentrations of all the species except the products (CO and H_2), are calculated by solving the rate of reactions associated with Eqs. 1–3 at steady state. The product species will leave the liquid phase immediately due to their low solubility. To facilitate the

(a)

(b)
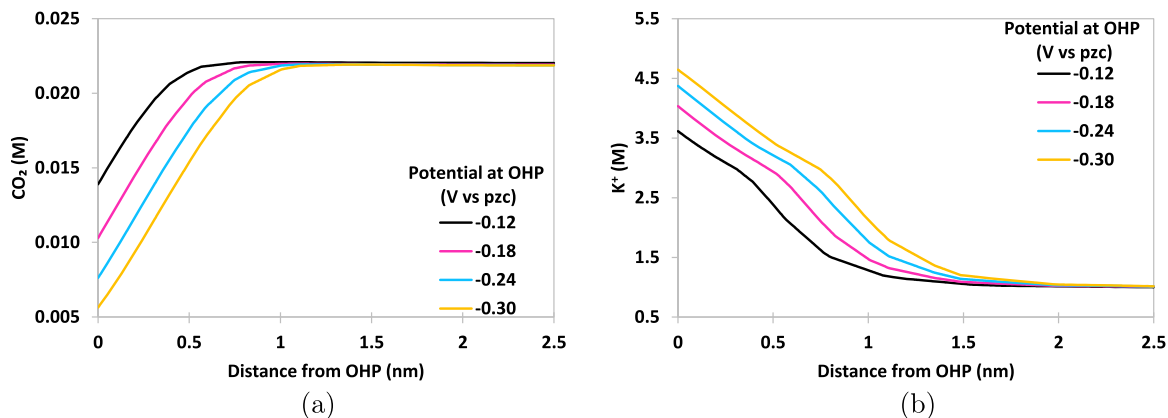
Figure 2. Radial variation of concentrations as a result of changing OHP potential (vs pzc) for an Ag (111) catalytic nanopore (R = 2.5 nm, L = 45 nm) in a 1.0 M KHCO$_3$ solution at I_{ECSA} = 2 mAcm^{-2} and 1 bar CO$_2$ pressure. (a) CO$_2$, (b) K$^+$.

simulations, an arbitrarily low value is set for the product species in the bulk of electrolyte. A more sophisticated approach can be coupled with the present model to simulate the mass transfer of these species into the bulk electrolyte. However, this would not influence the results presented in this study because these product species do not take part in the homogeneous reactions and they do not influence the electric field since they are charge neutral.[29] κ_{B5_i} is the convective mass transfer coefficient of species i, calculated as:

$$\kappa_{B5_i} = \frac{D_i}{L_c}\left(1.017\frac{2L_c}{L_{cross}}ReSc_i\right)^{\frac{1}{3}}. \qquad [21]$$

L_c is the length of the catalyst layer over which the electrolyte flows. L_{cross} is the width of the flow channel. Re and Sc represent the Reynolds and the Schmidt numbers, respectively, given by:

$$Re = \frac{\rho_{elec}L_c V_{elec}}{A_{cross}\mu_{elec}}, \qquad [22]$$

$$Sc_i = \frac{\mu_{elec}}{\rho_{elec}D_i}. \qquad [23]$$

A_{cross} is the electrolyte flow cross-section. V_{elec} is the flow rate and μ_{elec} is the viscosity of the electrolyte. The potential at the boundary B5 is set to 0:

$$\Phi_{B5} = 0. \qquad [24]$$

Other boundaries (B3, B4, B6).—For the remaining boundaries (B3, B4, B6), zero flux is assumed for the species' transport:

$$J_i^{B3,B4,B6} = 0. \qquad [25]$$

For the reservoir boundary B3, a fixed applied potential, similar to that at OHP (B2), is adopted in order to avoid a discontinuity in the potential at the interface between boundaries B2 and B3. Such a boundary condition is consistent with the properties of a conducting electrode.

$$\Phi_{B3} = E_{App}. \qquad [26]$$

For the remaining two boundaries (B4, B6), zero electric field is assumed:

$$\nabla\Phi = 0. \qquad [27]$$

Numerical solver details.—All concentrations will initially (t = 0) be at their bulk values throughout the domain. The OHP
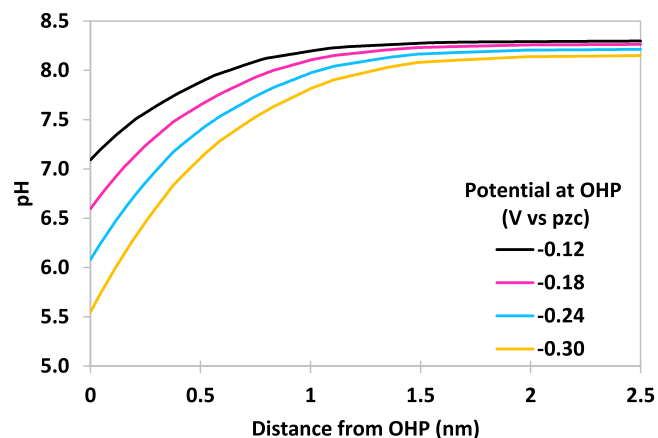
Figure 3. Radial variation of pH for different OHP potentials (vs pzc) for an Ag (111) catalytic nanopore (R = 2.5 nm, L = 45 nm) in a 1.0 M KHCO$_3$ solution at I_{ECSA} = 2 mAcm^{-2} and 1 bar CO$_2$ pressure.

potential is referenced with respect to the potential of zero charge (pzc) and ranges from −0.12 to −0.30 V vs pzc. The finite element package FEniCS is used to solve the weak formulation of the non-linear SMPNP equations. Temporal discretizations are carried out using the backward Euler scheme. A time step of 10^{-7} s is used until a steady state is attained. For the presented system, this time will be in milliseconds (supplementary results Fig. 7). Variable mesh spacing is used in the simulation domain, with finer mesh near the high-potential boundaries. To overcome instability, the potential values at boundaries B2 and B3 are increased in a step-wise manner. In the absence of a stepwise potential increase, extremely sharp potential gradients will be present in the initial stages of the simulation. A very small initial time step of $\approx 10^{-9}$ s (corresponding to the capacitative charging of EDL) would then be required to resolve the evolution of the potential profile.

Results and Discussion

In this section, we quantify the dependence of the local reaction environment on changes in key control parameters such as applied potential, bulk electrolyte concentration and pore radius. All radial profiles are evaluated at a distance of 25 nm from the gas/liquid interface B1.

Influence of applied potential.—Figure 2a represents the radial profile of CO$_2$ inside the nanopore against a range of applied potentials (−0.12 to −0.30 V vs pzc). The potential is applied at the OHP. It can be observed that the concentration of CO$_2$ remains
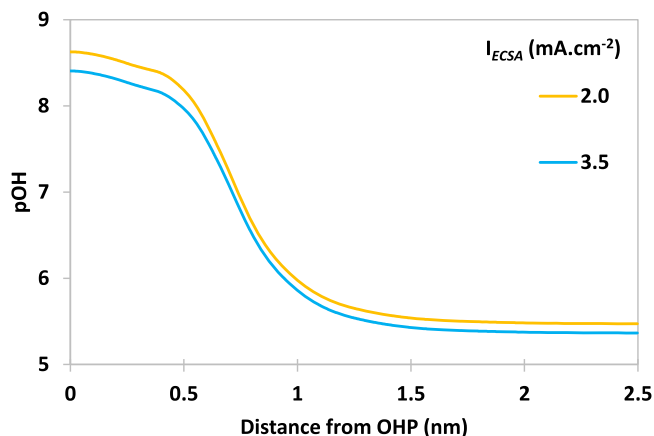
Figure 4. Radial variation of pOH as a result of changing I_{ECSA} for an Ag (111) catalytic nanopore (R = 2.5 nm, L = 45 nm) in a 1.0 M KHCO$_3$ solution at a fixed $\Phi_{OHP} = -0.24$ V vs pzc and 1 bar CO$_2$ pressure.

constant from the centre of the pore (2.5 nm) up to $\approx$1 nm away from the OHP, but decreases from this point onward. The radial drop in the CO$_2$ concentration is due to the presence of a dense layer of K$^+$ ions near the OHP. Electromigration drives K$^+$ ions to form a concentrated diffuse layer beyond the OHP. This imposes strong steric hindrances onto the CO$_2$ molecules based on Eq. 4, leading to a drop in CO$_2$ concentration near the electrode. Without these steric effects, pore models fail to capture the large radial variation of the CO$_2$ concentration.[22,46] This trend becomes even more pronounced at increasing applied potentials due to the fact that more K$^+$ ions are now attracted toward the OHP (Fig. 2b). This behavior was predicted by Bohra et al.[29] for a similar model; however, they did not observe an influence of steric effects in their pore model because their model was limited to very low applied potentials ($\approx$25 mV vs pzc). Figure 3 depicts the pH profile along the radial direction. A decline in the pH is observed as we move toward the reaction plane. This decline is caused primarily by the increased presence of H$^+$ ions in the vicinity of the OHP under negative applied potential. Furthermore, OH$^-$ ions are electrostatically repelled from the reaction plane, causing a drop in the local pH near the reactive surface. This effect increases with applied potential. Notably, CO$_2$ER studies often report an increase in local pH when going from the bulk toward the surface due to the production of OH$^-$ ions.[18,32]

We have seen that steric effects play an important role in the EDL at high applied surface potential. This also affects the interfacial pH. In the absence of steric effects (i.e. point charges assumption), there will be no limitation on the possible concentration of attracted H$^+$ ions near the OHP, leading to an underestimated

pH value at high applied potentials. It is also worth mentioning that the pH behavior in Figure 3 is based on a fixed current density value. In reality, the current density depends on the applied potential and is described by Butler-Volmer type kinetic expressions. A more sophisticated, microkinetic model might be necessary to accurately account for such reactions.[43] A higher current density results in a greater production rate of OH$^-$ as shown in Fig. 4. This would not change the trend of local pH within the EDL as the potential changes because the repulsion of OH$^-$ ions is the dominating factor.

Influence of bulk electrolyte concentration.—Figure 5a shows the influence of bulk electrolyte concentration on the radial concentration profile of CO$_2$. Increasing the electrolyte concentration from 0.01 M to 0.50 M KHCO$_3$ reduces the CO$_2$ concentration at the reaction plane. As shown in Fig. 2a, the interfacial CO$_2$ concentration decreases due to steric effects as more K$^+$ ions accumulate near the electrode (Fig. 5b). It can also be observed that beyond a certain distance from the OHP, the influence of the electric field and thus steric effects diminish and the concentrations reach their bulk values.

Apart from the steric effects, the electrolyte also affects the CO$_2$ concentration by reducing the dissolution of the incoming CO$_2$ at the gas/liquid interface. A higher electrolyte concentration would result in a lower CO$_2$ mass transfer rate across the B1 boundary based on the Sechenov correction of Henry's law.

The CO$_2$ mass transfer rate at B1 is calculated using Eq. 12, where $C_{CO_2}^{B1}$ is evaluated at every time step using the Sechenov-corrected Henry's law (see Eqs. 1–6 in the supplementary document). This relation depends on the ionic concentration of electrolytic species at the B1 interface. A higher ionic presence in the pore reduces the value of $C_{CO_2}^{B1}$, which in turn reduces the mass transfer rate of CO$_2$ across the interface.

In order to quantify this effect, we show the longitudinal variation of CO$_2$ concentration (Fig. 6). We take the measurement at the axisymmetry boundary (solid red line in Fig. 6b), which is the farthest away from the applied potential source. As a result, the steric effects would be the least at this boundary. We can observe that there is a linear drop in the CO$_2$ concentration from the gas/liquid interface at z = 0 nm until z = 45 nm for both electrolyte concentrations. This trend follows from a balance between the rate of CO$_2$ consumption and the rate at which CO$_2$ dissolves and diffuses back into the pore. The concentration of CO$_2$ at the gas/liquid interface already shows a significant difference for the two electrolyte concentrations used. The CO$_2$ concentration at this point (gas/liquid interface (z = 0) and axisymmetry axis (r = 0)) primarily depends on the ionic concentration inside the pore via the mass transfer condition in Eq. 12. Thus, for a high electrolyte concentration solution, we end up with an overall lower CO$_2$ concentration inside the pore.

(a)

(b)
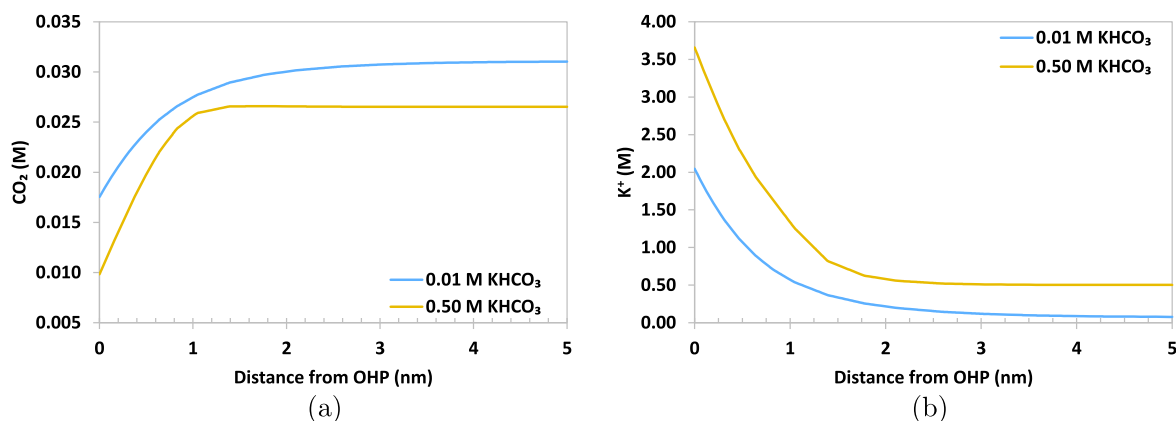
Figure 5. Radial concentration profiles for different electrolyte concentrations, for an Ag (111) catalytic nanopore (R = 5 nm, L = 45 nm), under $\Phi_{OHP} = -0.24$ V vs pzc at $I_{ECSA} = 2$ mAcm^{-2} and 1 bar CO$_2$ pressure.
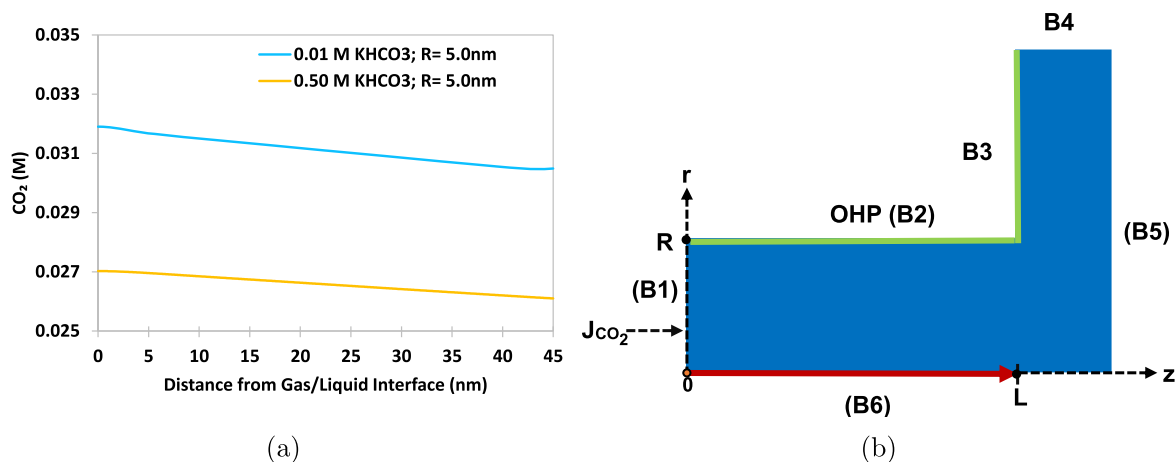
Figure 6. Longitudinal concentration profile of CO_2 taken at the axisymmetric axis (B6) as a result of changing electrolyte concentration, for an Ag (111) catalytic nanopore (R = 5 nm, L = 45 nm), under $\Phi_{OHP} = -0.24$ V vs pzc at $I_{ECSA} = 2$ mAcm^{-2} and 1 bar CO_2 pressure.
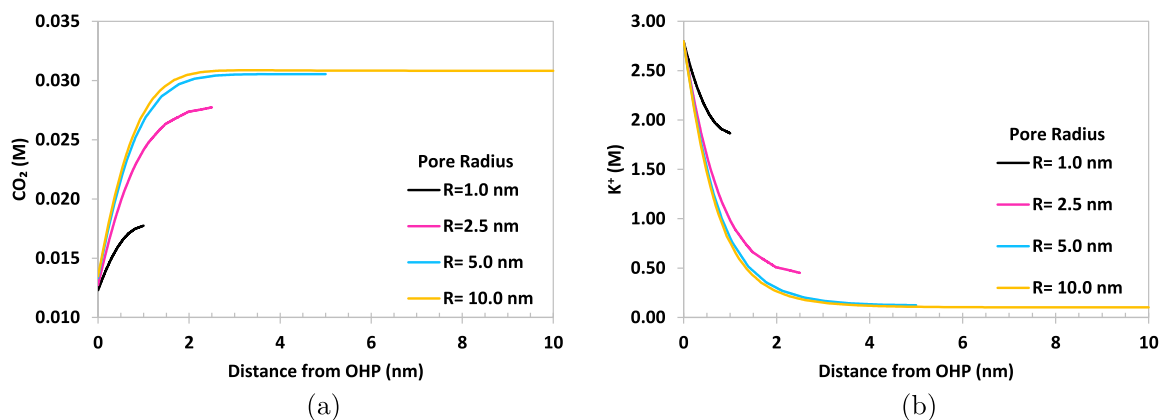
Figure 7. Radial variation of concentrations as a result of changing pore size for an Ag (111) catalytic nanopore in a 0.1 M KHCO$_3$ solution under $\Phi_{OHP} = -0.24$ V vs pzc, I_{ECSA} of 2 mAcm^{-2} and 1 bar CO_2 pressure.

Influence of pore diameter.—The influence of pore size on the radial CO_2 concentration profile can be seen in Fig. 7a. The radial profile is evaluated at a distance of z = 25 nm from the gas/liquid interface. Pore size has a negligible effect on CO_2 concentration at the reaction plane. This is because CO_2 concentration at high applied potentials largely depends on the concentration of K^+ ions. For a fixed value of Φ_{OHP} and bulk electrolyte concentration, the K^+ ions reach a concentration at the OHP that is independent of the pore size (Fig. 7b). However, moving away from the reaction plane, the K^+ concentration profiles for different pore sizes diverge.

The K^+ concentration in the centre of the pore increases when going from a larger pore radius of 10 nm to a smaller pore radius of 1 nm (Fig. 7b). This is because the mean potential inside the pore relative to the bulk potential is higher for a smaller pore compared to a larger-sized pore (supplementary results Fig. 2). This results in a stronger pull for K^+ ions from the bulk of electrolyte into the pore. This in turn lowers CO_2 concentration values. We can observe this behavior in Fig. 7a, where a smaller pore leads to a smaller mean CO_2 concentration inside the pore. For a pore radius of 5 nm and beyond, the concentration profiles become largely independent of the pore size. This is because the electric field gets screened near the reaction plane, as shown in supplementary Fig. 2. We can see that bulk potential values (=0 V vs pzc) are reached at the central axis of the pore (r = 0). This is why a similar concentration of K^+ is observed at the centre of both the 5 and 10 nm pores. The higher

mean cation concentrations in larger pores, in turn, influence the homogeneous reactions and the average pH inside the pore.

Figure 8a shows the radial variation of pH for various pore sizes in a 0.5 M KHCO$_3$ solution. Based purely on the idea of smaller pores having a higher mean potential, the expected trend in pH should be opposite to the trend in K^+ concentration shown in Fig. 7b. A higher mean potential inside the pore should result in a higher concentration of H^+ ions and, thus a lower pH. This trend can indeed be observed in Fig. 8a, when looking at the pores of at least 2.5 nm radius. These pores show a slight increase in the interfacial pH with an increasing pore size. However, the pore of 1 nm radius completely deviates from this trend by showing a higher interfacial pH than each of the larger pores. This is because, besides the mean potential, there are several other competing phenomena that influence the overall makeup of the pH. For example, a smaller pore would have a lower mean CO_2 concentration (Fig. 7a), this would lead to a decrease in bicarbonate production and consequently a decrease in the consumption of OH^- ions (Eq. 1), making the pore more basic. Furthermore, a smaller pore would have a higher surface-to-volume ratio; hence, for a fixed I_{ECSA} value, a smaller pore would have a higher mean OH^- concentration. Another factor to consider is that the potential drop from the OHP to the centre of the pore is extremely small for the pore of 1 nm radius. Consequently, this would result in a more basic pore via the decreased overall pull for H^+ ions toward the reaction plane. This
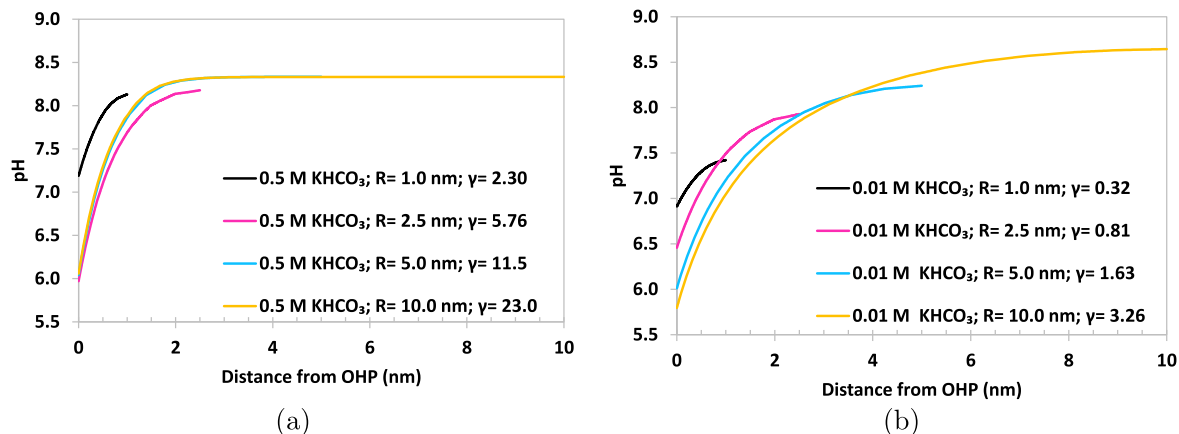
Figure 8. Radial variation of pH as a result of changing pore size for an Ag (111) catalytic nanopore under $\Phi_{OHP} = -0.24$ V vs pzc, I_{ECSA} of 2 mAcm^{-2} and 1 bar CO_2 pressure. (a) 0.5 M KHCO$_3$ solution, (b) 0.01 M KHCO$_3$ solution.

behavior can be modulated by the ratio:

$$\gamma = \frac{R}{\lambda_{Debye}}. \qquad [28]$$

Here, R is the radius of the pore (upto the OHP) and λ_{Debye} is the Debye length, defined as:

$$\lambda_{Debye} = \sqrt{\frac{\epsilon_0 \epsilon_r^0 k_B T}{2\epsilon_0^2 C_{elec} N_A}}. \qquad [29]$$

k_B is Boltzmann's constant and C_{elec} is the concentration of the electrolyte. When γ is ≈ 2.3 (for 1 nm pore in Fig. 8a) or less, the influence of the mean potential is expected to be less relevant compared to the counteracting phenomena discussed above, resulting in pores becoming more basic as seen in the case of the 1 nm pore in Fig. 8a. To test this theory, we lower the electrolyte concentration from 0.5 M to 0.01 M KHCO$_3$ (Fig. 8b). This increases the Debye length from $\lambda_{Debye} \approx 0.43$ nm to $\lambda_{Debye} \approx 3$ nm and consequently decreases γ. As a result, pores of radius 2.5 nm and 5 nm, both show a more basic pH trend near the reaction plane as compared to the 10 nm pore. Considering the importance of the local pH in maintaining a favourable reaction environment inside the pore, the ratio γ can provide crucial insight into the optimal design of a GDE. One can regulate the ratio by varying either the pore size or the ionic strength of the system, in order to get a desired pH trend inside the catalyst layer.

The presented GDE model involves multiscale mass transport coupled with homogeneous and heterogeneous reactions. Our pore-scale model describes the mass transport in the pore subject to imposed reaction rates. It can be used to predict the local environment inside the EDL of the pore. This model could be coupled to descriptions of the larger length scales as well as an explicit description of the molecular transport and reaction processes on the smaller scales. The pore model can be seamlessly integrated with a gas transport model such as convection and mixed average diffusion model[18,22] to account for the GDL. The GDL model will inform the amount of gaseous species at the gas/liquid interface (Eqs. 11–12).

The 2D pore-scale model can also be coupled to a microkinetic model to[43,47] to quantify the influence of GDE structural properties on faradaic efficiencies of the desired products. If the rate-determining steps of the CO$_2$ER reactions are known, then a simplified Frumkin-corrected Tafel relation can also be used to get an accurate estimation of the current densities.[31,48–51] Currently, the model does not account for the specific adsorption of ions on the surface of the catalyst. This is theorized to have an impact on the concentration and potential profiles.[27,52,53] Even though the continuum hypothesis does hold for the smallest pore size used in this work (which has a

diameter of 2 nm, excluding the Stern layer),[54] the consequence of not being able to capture the exact molecular effects at the surface, including ion-ion correlations, may be substantial in this smallest pore due to the large surface-to-volume ratio. A coupled approach with molecular dynamics simulation should be developed to inform the continuum scale transport models.

Conclusions

This work presents a 2D GDE nanopore model for CO$_2$ER based on a set of size-modified PNP equations. Traditionally, GDE models for CO$_2$ER tend to ignore the formation of the EDL and hence fail to accurately describe the local environment such as concentration profiles and pH inside the pore. Our approach overcomes this limitation by incorporating the EDL region near the reaction plane.

The study was performed based on Ag(111) catalyst in contact with a KHCO$_3$ solution. Our model predicts a significant drop in the CO$_2$ concentration near the reaction plane due to the high local concentration of K$^+$ ions. This effect increases with applied cathodic potentials. Most of the literature on GDE models for CO$_2$ER fail to account for this drop that is induced by steric effects. We also observed a drop in pH going from the centre of the pore to the reaction plane. This is because the region near the OHP has a stronger electric field and thus a stronger pull for H$^+$ ions relative to the centre of the pore. The attraction of H$^+$ ions inside the pore and repulsion for OH$^-$ ions from the walls of the pore increase with cathodic potentials, making the pore more acidic at higher potentials. The CO$_2$ concentration inside the pore also drops with increased electrolyte concentration due to both increased steric effects as well as due to the decreased dissolution of CO$_2$ in the liquid phase. This decrease was quantified using the Sechenov-corrected Henry's law.

The model also describes the influence of pore size on the local environment. Four different pore sizes were simulated. The difference in CO$_2$ and cation concentration at the reaction plane is found to be independent of the pore size, while the smaller pores showed a higher mean cation concentration relative to a larger pore due to a greater potential difference between the pore and the bulk of electrolyte. This increases the steric repulsion for CO$_2$ and thus a decreased mean concentration is observed for CO$_2$ in a smaller pore. The effect of pore size on the pH is, however, not entirely dictated by the mean potential as several competing phenomena can influence the local pH. For example, even if the potential value at any given point is high in a smaller pore, making the pore more acidic, the carbonate balance and increased surface-to-volume ratio would impart a more basic character to the pore. This is why a pore radius of 1 nm shows a more basic pH near the reaction plane compared to larger pores. The γ factor, which is the ratio between the pore radius and the Debye length, can be used to predict the pH trend. Below the threshold value of 2.3, even pores of 2.5 and 5 nm radius became

more basic near the reaction plane than the larger 10 nm pore. This factor can be extremely useful for researchers focusing on the optimal structural design of the pore as it allows them to regulate the pH trend inside the catalyst layer of a CO_2ER process.

The cost-effective methodology presented in this work allows us to gain key insights into the local environment within a nanopore and can be used to make informed decisions regarding the inputs for larger pore network models.

ORCID

Esaar N. Butt https://orcid.org/0000-0002-5050-7649
Johan T. Padding https://orcid.org/0000-0003-4161-0748
Remco Hartkamp https://orcid.org/0000-0001-8746-8244

References

1. W. A. Smith, T. Burdyny, D. A. Vermaas, and H. Geerlings, "Pathways to industrial-scale fuel out of thin air from CO_2 electrolysis." *Joule*, **3**, 1822 (2019).
2. Z. Yan, J. L. Hitt, J. A. Turner, and T. E. Mallouk, "Renewable electricity storage using electrolysis." *Proc. Natl. Acad. Sci. U.S.A.*, **117**, 12558 (2020).
3. X. Lu, D. Y. Leung, H. Wang, M. K. Leung, and J. Xuan, "Electrochemical reduction of carbon dioxide to formic acid." *ChemElectroChem*, **1**, 836 (2014).
4. E. Ruiz-López, J. Gandara-Loe, F. Baena-Moreno, T. R. Reina, and J. A. Odriozola, "Electrocatalytic CO_2 conversion to C_2 products: Catalysts design, market perspectives and techno-economic aspects." *Renew. Sust. Energ. Rev.*, **161**, 112329 (2022).
5. D. T. Whipple and P. J. A. Kenis, "Prospects of CO_2 utilization via direct heterogeneous electrochemical reduction." *J. Phys. Chem. Lett.*, **1**, 3451 (2010).
6. S. Niphadkar, P. Bagade, and S. Ahmed, "Bioethanol production: insight into past, present and future perspectives." *Biofuels*, **9**, 229 (2018).
7. J. Albo and A. Irabien, "Cu_2O-loaded gas diffusion electrodes for the continuous electrochemical reduction of CO_2 to methanol." *J. Catal.*, **343**, 232 (2016).
8. M. Heelmann, B. C. Bräsel, R. G. Keller, and M. Wessling, "Simulation-based guidance for improving CO_2 reduction on silver gas diffusion electrodes." *Electrochemical Science Advances*, **3**, 2100160 (2023).
9. J. C. Bui, E. W. Lees, L. M. Pant, I. V. Zenyuk, A. T. Bell, and A. Z. Weber, "Continuum modeling of porous electrodes for electrochemical synthesis." *Chem. Rev.*, **122**, 11022 (2022).
10. K. Malik, B. M. Rajbongshi, and A. Verma, "Syngas production from electrochemical reduction of CO_2 at high current density using oxide derived Zn/Cu nanocomposite." *J. CO_2 Util.*, **33**, 311 (2019).
11. J. Albo, D. Vallejo, G. Beobide, O. Castillo, P. Castaño, and A. Irabien, "Copper-based metal-organic porous materials for CO_2 electrocatalytic reduction to alcohols." *ChemSusChem*, **10**, 1100 (2017).
12. C.-T. Dinh et al., "CO_2 electroreduction to ethylene via hydroxide-mediated copper catalysis at an abrupt interface." *Science*, **360**, 783 (2018).
13. S. Verma, X. Lu, S. Ma, R. I. Maseld, and P. J. A. Kenis, "The effect of electrolyte composition on the electroreduction of CO_2 to CO on Ag based gas diffusion electrodes." *Phys. Chem. Chem. Phys.*, **18**, 7075 (2016).
14. C. Delacourt, P. L. Ridgway1, J. B. Kerr, and J. Newman, "Design of an electrochemical cell making syngas (CO+H_2) from CO_2 and H_2O reduction at room temperature." *J. Electrochem. Soc.*, **155**, B42 (2008).
15. J. Wu et al., "A metal-free electrocatalyst for carbon dioxide reduction to multi-carbon hydrocarbons and oxygenates." *Nat. Commun.*, **7**, 13869 (2016).
16. C. M. Gabardo, A. Seifitokaldani, J. P. Edwards, C.-T. Dinh, T. Burdyny, M. G. Kibria, C. P. O'Brien, E. H. S. ORCID, and D. Sinton, "Combined high alkalinity and pressurization enable efficient CO_2 electroreduction to CO." *Energy Environ. Sci.*, **11**, 2531 (2018).
17. J.-J. Lv, M. Jouny, W. Luc, W. Zhu, J.-J. Zhu, and F. Jiao, "A highly porous copper electrocatalyst for carbon dioxide reduction." *Adv. Mater.*, **30**, 1803111 (2018).
18. L.-C. Weng, A. T. Bell, and A. Z. Weber, "Modeling gas-diffusion electrodes for CO_2 reduction." *Phys. Chem. Chem. Phys.*, **20**, 16973 (2018).
19. Y. C. Tan, K. B. Lee, H. Song, and J. Oh, "Modulating local CO_2 concentration as a general strategy for enhancing C C coupling in CO_2 electroreduction." *Joule*, **4**, 1104 (2020).
20. L. C. Brée, M. Wessling, and A. Mitsos, "Modeling and simulating electrochemical reduction of CO_2 in a microfluidic cell." *Computers and Chemical Engineering*, **139**, 106890 (2020).
21. Y. Kotb, S.-E. K. Fateen, J. Albo, and I. Ismail, "Modeling of a microfluidic electrochemical cell for the electro-reduction of CO_2 to CH_3OH." *J. Electrochem. Soc.*, **164**, E391 (2017).
22. R. Kas, A. G. Star, K. Yang, T. V. Cleve, K. C. Neyerlin, and W. A. Smith, "Along the channel gradients impact on the spatioactivity of gas diffusion electrodes at high conversions during CO_2 electroreduction." *ACS Sustainable Chemistry and Engineering*, **9**, 1286 (2021).
23. O. A. El-Shafie, R. M. El-Maghraby, J. Albo, S.-E. K. Fateen, and A. Abdelghany, "Modeling and numerical investigation of the performance of gas diffusion electrodes for the electrochemical reduction of carbon dioxide to methanol." *Ind. Eng. Chem. Res.*, **59**, 20929 (2020).
24. J. W. Blake, V. Konderla, L. M. Baumgartner, D. A. Vermaas, J. T. Padding, and J. W. Haverkort, "Inhomogeneities in the catholyte channel limit the upscaling of CO_2 flow electrolysers." *ACS Sustainable Chemistry and Engineering*, **11**, 2840 (2023).
25. G. O. Larrazábal, A. J. Martín, and J. Pérez-Ramírez, "Building blocks for high performance in electrocatalytic CO_2 reduction: materials, optimization strategies, and device engineering." *J. Phys. Chem. Lett.*, **8**, 3933 (2017).
26. M. Liu et al., "Enhanced electrocatalytic CO_2 reduction via field-induced reagent concentration." *Nature*, **537**, 382 (2016).
27. D. Bohra, J. H. Chaudhry, T. Burdyny, E. A. Pidko, and W. A. Smith, "Modeling the electrical double layer to understand the reaction environment in a CO_2 electrocatalytic system." *Energy Environ. Sci.*, **12**, 3380 (2019).
28. J. Resasco, L. D. Chen, E. Clark, C. Tsai, C. Hahn, T. F. Jaramillo, K. Chan, and A. T. Bell, "Promoter effects of alkali metal cations on the electrochemical reduction of carbon dioxide." *J. Am. Chem. Soc.*, **139**, 11277 (2017).
29. D. Bohra, J. H. Chaudhry, T. Burdyny, E. A. Pidko, and W. A. Smith, "Mass transport in catalytic pores of GDE-based CO_2 electroreduction systems." *ChemRxiv*, **1**, 1 (2020).
30. J. Hussain, H. Jónsson, and E. Skúlason, "Calculations of product selectivity in electrochemical CO_2 reduction." *ACS Catal.*, **8**, 5240 (2018).
31. E. N. Butt, J. T. Padding, and R. Hartkamp, "Size-modified Poisson-Nernst-Planck approach for modeling a local electrode environment in CO_2 electrolysis." *Sustainable Energy and Fuels*, **7**, 144 (2022).
32. J. Blake, J. Padding, and J. Haverkort, "Analytical modelling of CO_2 reduction in gas-diffusion electrode catalyst layers." *Electrochim. Acta*, **393**, 138987 (2021).
33. M. Z. Bazant, M. S. Kilic, B. D. Storey, and A. Ajdari, "Towards an understanding of induced-charge electrokinetics at large applied voltages in concentrated solutions." *Adv. Colloid Interface Sci.*, **152**, 48 (2009).
34. M. S. Kilic, M. Z. Bazant, and A. Ajdari, "Steric effects in the dynamics of electrolytes at large applied voltages. I. Double-layer charging." *Physical Review E—Statistical, Nonlinear, and Soft Matter Physics*, **75**, 1 (2007).
35. M. S. Kilic, M. Z. Bazant, and A. Ajdari, "Steric effects in the dynamics of electrolytes at large applied voltages. II. Modified Poisson-Nernst-Planck equations." *Physical Review E—Statistical, Nonlinear, and Soft Matter Physics*, **75**, 021503 (2007).
36. M. Z. Bazant, K. T. Chu, and B. J. Bayly, "Current-voltage relations for electrochemical thin films." *SIAM Journal on Applied Mathematics*, **65**, 1463 (2005).
37. A. Bonnefont, F. Argoul, and M. Z. Bazant, "Analysis of diffuse-layer effects on time-dependent interfacial kinetics." *Journal of Electroanalytical Chemistry*, **500**, 52 (2001).
38. H. Wang, A. Thiele, and L. Pilon, "Simulations of cyclic voltammetry for electric double layers in asymmetric electrolytes: a generalized modified Poisson-Nernst-Planck model." *J. Phys. Chem. C*, **117**, 18286 (2013).
39. B. Lu and Y. C. Zhou, "Poisson-Nernst-Planck equations for simulating biomolecular diffusion-reaction processes II: Size effects on ionic distributions and diffusion-reaction rates." *Biophys. J.*, **100**, 2475 (2011).
40. K. Willems, D. Ruic, F. L. Lucas, U. Barman, N. Verellen, J. Hofkens, G. Maglia, and P. V. Dorpe, "Accurate modeling of a biological nanopore with an extended continuum framework." *Nanoscale*, **12**, 16775 (2020).
41. J. B. Hasted, D. M. Ritson, and C. H. Collie, "Dielectric properties of aqueous ionic solutions. parts I and II." *The Journal of Chemical Physics*, **16**, 1 (1948).
42. J. Bockris and A. Reddy, *Modern Electrochemistry* (Springer, New York, NY) 2nd ed. (1998).
43. S. Ringe, C. G. Morales-Guio, L. D. Chen, M. Fields, T. F. Jaramillo, C. Hahn, and K. Chan, "Double layer charging driven carbon dioxide adsorption limits the rate of electrochemical carbon dioxide reduction on Gold." *Nat. Commun.*, **11**, 33 (2020).
44. S. Weisenberger and A. Schumpe, "Estimation of gas solubilities in salt solutions at temperatures from 273 K to 363 K." *AIChE J.*, **42**, 298 (1996).
45. T. Burdyny, P. J. Graham, Y. Pang, C.-T. Dinh, M. Liu, E. H. Sargent, and D. Sinton, "Nanomorphology-enhanced gas-evolution intensifies CO_2 reduction electrochemistry." *ACS Sustainable Chemistry and Engineering*, **5**, 4031 (2017).
46. T. Moore, X. Xia, S. E. Baker, E. B. Duoss, and V. A. Beck, "Elucidating mass transport regimes in gas diffusion electrodes for CO_2 electroreduction." *ACS Energy Lett.*, **6**, 3600 (2021).
47. X. Zhu, J. Huang, and M. Eikerling, "Electrochemical CO_2 Reduction at Silver from a Local Perspective." *ACS Catal.*, **11**, 14521 (2021).
48. A. Frumkin, "Wasserstoffuberspannung und struktur der doppelschicht." *Zeitschrift für physikalische Chemie*, **164**, 121 (1933).
49. R. Parsons, "Structure of the electrical double layer and its influence on the rates of electrode reactions." *Advances in Electrochem. Electrochem. Eng.*, **1**, 1 (1961).
50. M. Rossi, T. Wallmersperger, S. Neukamm, and K. Padberg-Gehle, "Modeling and simulation of electrochemical cells under applied voltage." *Electrochimica Acta*, **258**, 241 (2017).
51. P. M. Biesheuvel, M. van Soestbergen, and M. Z. Bazant, "Imposed currents in galvanic cells." *Electrochimica Acta*, **54**, 4857 (2009).
52. M. F. Döpke and R. Hartkamp, "The importance of specifically adsorbed ions for electrokinetic phenomena: Bridging the gap between experiments and MD simulations." *J. Chem. Phys.*, **154**, 094701 (2021).
53. R. Hartkamp, A.-L. Biance, L. Fu, J.-F. Dufrêche, O. Bonhomme, and L. Joly, "Measuring surface charge: why experimental characterization and molecular modeling should be coupled." *Current Opinion in Colloid and Interface Science.*, **37**, 101 (2018).
54. L. Bocquet and E. Charlaix, "Nanofluidics, from bulk to interfaces." *Chem. Soc. Rev.*, **39**, 1073 (2010).